J. Fluid Mech. (1980). *vol.* 98, *part* 1, *pp.* 65–95
Printed in Great Britain

A 'turbulent spot' in an axisymmetric free shear layer. Part 1

By M. SOKOLOV, A. K. M. F. HUSSAIN, S. J. KLEIS AND Z. D. HUSAIN

Department of Mechanical Engineering, University of Houston, Texas 77004

(Received 26 September 1978 and in revised form 2 February 1979)

A three-dimensional 'turbulent spot' has been induced in the axisymmetric free mixing layer of a 12·7 cm diameter air jet by a spark generated at the nozzle boundary layer upstream of the exit. The spot coherent-structure signature, buried in the large-amplitude random fluctuating signal, has been educed at three downstream stations within the apparent self-preserving region of the mixing layer (i.e. $x/D = 1{\cdot}5$, 3·0 and 4·5) at the jet exit speed of $20\,\mathrm{m\,s^{-1}}$. The eduction has been performed through digital phase averaging of the spot signature from 200 realizations. In order to reduce the effect of the turbulence-induced jitter on the phase average, individual filtered signal arrays were optimally time-aligned through an iterative process of cross-correlation of each realization with the ensemble average. Further signal enhancement was achieved through rejection of realizations requiring excessive time shifts for alignment. The number of iterations required and the fraction of realizations rejected progressively increase with the downstream distance and the radial position.

The mixing-layer spot is a large-scale elongated structure spanning the entire width of the layer but does not appear to exhibit a self-similar shape. The dynamics of the mixing-layer spot and its eduction are more complicated than those of the boundary-layer spot. The spot initially moves downstream essentially at a uniform speed across the mixing layer, but further downstream it accelerates on the high-speed side and decelerates on the low-speed side. This paper discusses the data acquisition and processing techniques and the results based on the streamwise velocity signals. Phase average distributions of vorticity, pseudo-streamlines, coherent and background Reynolds stresses and further dynamics of the spot are presented in part 2 (Hussain, Kleis & Sokolov 1980).

1. Introduction

Even though the presence as well as significance of large-scale coherent structures in turbulent shear flows were recognized early and in a few cases, investigated previously (Townsend 1956; Mollo-Christensen 1967; Landahl 1967; Kline *et al.* 1967; Payne & Lumley 1967; Hussain & Reynolds 1970), the unusually high contemporary interest in these structures has been spurred by the recent discovery of the quasi-deterministic nature of these structures and their mutual interactions (Brown & Roshko 1974; Winant & Browand 1974; Crow & Champagne 1971; Moore & Saffman 1975; Hussain & Zaman 1975) and the expectation that knowledge of these structures may be crucial to the understanding and modelling of shear-flow turbulence (Phillips 1967; Reynolds

0022-1120/80/4436-8640 $02.00

& Hussain 1972; Roshko 1976; Liepmann 1978; Saffman 1978; Kovasznay 1978). Recent research advances continue to suggest that the large-scale coherent structures and their interactions play a significant role in the transport of momentum, heat and mass (in flows which have all the characteristics of fully-developed turbulence) and, presumably, in jet noise production (Maestrello 1977, private communication; Ffowcs Williams & Kempton 1978). While these structures are likely to be important in both wall-bounded (external and internal) and wall-free shear flows, they appear to be more pronounced in the latter.

The isothermal, incompressible, single-phase free shear layer of a Newtonian fluid is probably the simplest practical turbulent shear flow and, as such, has been the fertile ground for a number of recent and continuing investigations. The concepts of asymptotic and local invariances suggest that the flow structure sufficiently downstream from the origin should be universal. Accumulated data in the incompressible free shear layer, however, reveal widespread discrepancy even in its characteristic integral measures (Birch & Eggers 1973; Champagne, Pao & Wygnanski 1976; Hussain & Zedan 1978*a*), thus pointing to the lack of understanding of even this simplest flow, the inherent complexity of shear flow turbulence, and the need for additional careful measurements in this flow.

When the Reynolds number is sufficiently high, the turbulent free-shear layer can only be a function of the boundary and initial conditions which can affect the formation of the coherent structures (through the shear-layer instability, saturation, and roll-up) as well as their evolution and even successive interactions. Also, if the shear flow dynamics is controlled by the coherent structures and their interactions (Winant & Browand 1974), the initial condition can continue to retain some influence on the flow downstream. Thus, the concept of (coherent structure) equilibrium must be relegated to the asymptotic far field, not likely achievable in a laboratory experiment (Foss 1977; Fiedler & Thies 1978; Hussain 1978). Earlier investigations (Bradshaw 1966; Clark 1974) suggested that the widespread discrepancies between different previous investigations might be primarily due to different initial conditions existing in the apparatus used. While the average measures of the shear layer tend to support this speculation (Batt 1975; Foss 1977; Hussain & Zedan 1978*a*, *b*), the true explanation will probably depend on the detailed dynamics of the large-scale coherent structure. The boundary condition can also affect the coherent structure interaction through feedback mechanisms (Dimotakis & Brown 1976; Hussain & Zaman 1978*b*).

The coherent structures are typically stronger (owing to larger gradients of vorticity) in the near fields of free flows than in their far fields, the near field being also relevant to the majority of technological applications including mixing and noise production. In fact, the possible existence and role of the large-scale coherent structure in the far-field of a circular jet is still an open question. Even though a number of investigations (Ko & Davies 1971; Lau & Fisher 1975; Michalke & Fuchs 1975) have been addressed to the coherent structures in the near-field of a circular jet, detection of these structures in an uncontrolled flow is complex and not free from ambiguity (Bruun 1977; Lau 1978, private communication; Leuchter 1978, private communication). An alternative approach is to organize the formation of these otherwise randomly occurring structures and their interactions through controlled excitation (Crow & Champagne 1971; Bechert & Pfizenmaier 1975; Moore 1977; Hussain & Zaman 1978*a*). These excitations in a circular jet introduce two-dimensional (axisymmetric) coherent structures which,

however, may become three-dimensional downstream (Yule 1977; Davies & Baxter 1978; Zaman 1978). In contrast with the initially two-dimensional structure, practically plane and axisymmetric mixing layers develop strong three-dimensionality which may control its transport and noise production characteristics.

Our motivation was, therefore, to study the evolution of a three-dimensional perturbation of the initial condition and study the evolution of the disturbance in the mixing layer. It was decided to introduce the three-dimensional disturbance with the help of a spark and record the evolution of the spot induced by it. The axisymmetric mixing layer is the ideal two-dimensional mixing layer in the sense that it is free from the otherwise inherent three-dimensional end effects. Additionally, the availability of a large size (12·7 cm diameter) air jet and the ease of attachment of the spark generator influenced the choice of the axisymmetric mixing layer. The inherently limited streamwise extent of the axisymmetric layer is not a constraint since we are interested in the initial evolution of the 'turbulent spot'.

To our knowledge, this is the first study of a spark-induced spot in the free mixing layer, even though similar studies have been performed in wall boundary layers (Wygnanski, Sokolov & Friedman 1976; Zilberman, Wygnanski & Kaplan 1977; Coles & Barker 1975; Cantwell, Coles & Dimotakis 1978) where the spot study has been motivated by the 'bursting' phenomenon; the spots in the latter two studies, however, were induced by a jet perturbation through the wall. It is expected that the evolution of a spot in a free shear layer, apart from being an interesting basic problem itself, is not too different from the evolution of a naturally occurring three-dimensional coherent structure in the free shear layer. One inherent difference is that in a mixing layer the initial large-scale structure is two-dimensional even though the flow eventually develops three-dimensionality (Yule 1977; Davies & Baxter 1978; Zaman 1978; Chandrsuda *et al.* 1978; Clark 1979). In the present experiment we start with an initially three-dimensional disturbance induced by the spark.

The objective of this study was to generate a spark in the boundary layer preceding the lip, to use the spark trigger as a time reference for phase-locked measurements of the spot-induced motion, to educe the spot geometry and flow structure from hot-wire signals containing its signature, and to study the evolution and distortion of the spot coherent structure and its role in turbulence transport. In this part we report the coherent structure eduction techniques together with the longitudinal velocity measurements for a single spot in the initially laminar shear layer. The cases of initially turbulent boundary layer, multiple spots, as well as the phase average measurements of intermittency, Reynolds stress, pseudo-streamlines, and vorticity of the spot coherent structure, will be addressed in subsequent studies.

2. Apparatus

The spot was studied in the axisymmetric free shear layer of a 12·7 cm diameter air jet at an exit velocity of 20 m s^{-1} (figure 1). The facility consists of a number of modules connected by flexible rubber membranes. Air from a filter box (which removes 95 % of 0·5 μm diameter particles) enters the six-blade centrifugal blower driven by a d.c. motor. The motor–blower assembly is mounted on flexible neoprene mountings for isolating its vibrations. The d.c. motor control (designed in our laboratory) consists of three-phase armature and single-phase field full-wave rectifier circuits, providing

independent voltage controls by motor-driven variacs. The tunnel operation is thus free from both motor speed variations and associated acoustic noise typical of SCR-controlled drives, especially at low speeds. The jet exit speed U_e can be varied continuously from 3 to 80 m s^{-1} and held constant at any desired speed to less than 1 % variation. Air from the blower flows through a 1·0 m long muffler box designed to suppress high-frequency acoustic components. Following the muffler box is a 1·3 m long straightener box of rectangular cross-section (33 × 26 cm) attached with a slit-type Helmholtz resonator and four adjustable quarter-wave tubes, designed to suppress blade passage and tunnel-cavity resonance frequencies.

The flow then passes through a 12° square diffuser fitted with an inlet screen, an exit screen, and two screens in the middle, thus dividing the diffuser into three equal-length chambers. A straight square section followed by a square-to-round transfer box, each 0·7 m long, connects the diffuser to the 76·2 cm diameter settling chamber, 2·8 m in length and fitted with a honeycomb and ten screens. The flow emerges in the laboratory through an axisymmetric nozzle (36: 1 contraction ratio) made of fibre-glass. The nozzle is 76 cm long and has a contour which is a compromise between the Batchelor–Shaw and the cubic equation shapes (Hussain & Ramjee 1976). The nozzle is terminated with a metal ring which accepts nozzle tips of various lengths and various trip rings. Further details of the apparatus have been given by Husain & Hussain (1979).

The flow emerges from an aluminium tip with a wedge angle of 20° at the end of the nozzle. The spark is generated between two needles projecting through a (4·8 cm diameter) Bakelite insert in the tip so that the two needles are insulated from each other and from the tip. The two needles (0·085 cm diameter), located at 6·8 cm upstream from the nozzle exit, are separated by a spanwise gap of 1·4 cm and project inside the tip wall by 0·5 mm. The tip with the Bakelite insert was machined hydraulically smooth. The spark between the two needles is generated when a voltage of 35 kV is imposed across the needle-gap. The voltage is triggered by a function generator and generated by an ordinary ignition coil. The function generator provides control of the period between sparks as well as the time reference for the appropriate time delay between the spark trigger and initiation of on-line computer-controlled data acquisition so that the recorded data array captures the spot signature.

The jet discharges into a large laboratory (30 × 15 × 3·5 m) with controlled temperature, humidity and traffic. The hot-wire traverse, with a resolution of 0·0254 mm, is performed by a four-co-ordinate (x, y, z, ϕ) automated traversing mechanism (backlash free) operated by stepping motors under software control from the on-line laboratory computer (HP 2100S) located in an adjoining room. The discharge of the jet in a large laboratory and remote control of probe traverse and data acquisition assured that the free shear layer was relatively free from external disturbances; the ambient turbulence intensity was not recorded. Analog data are transmitted to the computer through a 25 m long cable provided with a termination network so that the signal is free from distortion and reflexion up to 100 kHz. Data were digitized with the help of a 12-bit A/D converter (204 kHz maximum sampling rate) built in house.

Data were obtained with a TSIX-wire probe using 2 mm long 4 μm tungsten wires with Disa model 55M anemometers and 55D10 linearizers. In addition to the linearized hot-wire signals, the computer read a trigger signal (time delayed from the spark generation) and an intermittency signal. Each wire was calibrated by least-square fitting a

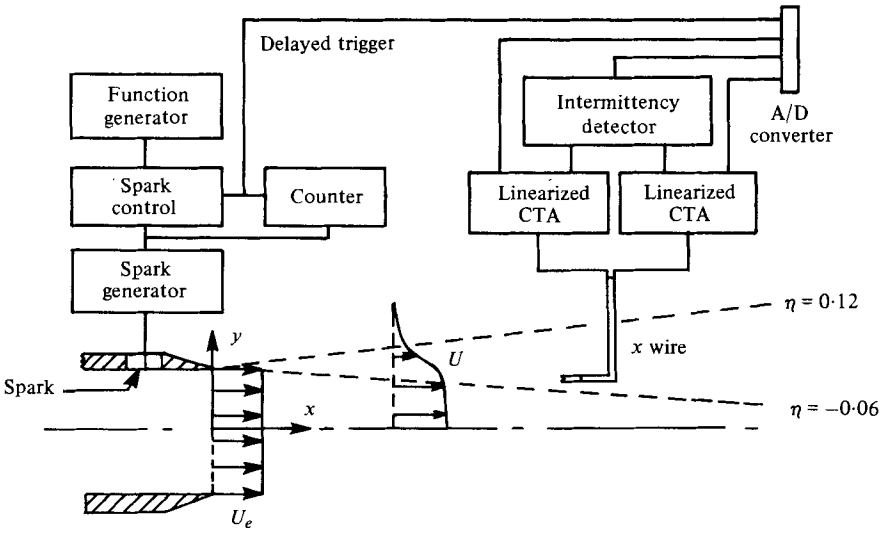

FIGURE 1. Schematic of the measurement region and instrumentation.

cubic equation to fifty equally-spaced velocity data points from zero velocity to 150 % of the jet exit velocity used. These cubic equations were used for all linearized signals (i.e. linearizers were used but calibration linearity was not assumed).

Two types of data were obtained simultaneously. The two x-wire outputs and intermittency signals (presented in part 2) were stored as time records for each realization for later processing. Between sparks (approximately 1 second apart), long-term time averages of each wire and the squares and cross-product of the two signals were computed and used with the calibration coefficients to obtain time-mean quantities for the undisturbed flow. The sampling rate for the time-averaged signals was 4·2 kHz and for the disturbance time record was 8·4 kHz per signal; each signal realization was about 60 ms long, containing 500 data points. The uncertainty in initiating the high-speed data sampling was 0·32 ms; this is the 'turn on' time for the A/D converter after it is activated by the delayed trigger signal. The schematic of the flow region, the associated instrumentation and the co-ordinates used are shown in figure 1.

3. Results and discussion

This experiment has been carried out with an initially untripped boundary layer at an exit speed $U_e = 20\,\mathrm{m\,s^{-1}}$ corresponding to the jet Reynolds number of

$$Re_D = 1{\cdot}8 \times 10^5.$$

The exit free-stream fluctuation intensity was 0·34 %. This paper describes measurement of the streamwise velocity associated with a single spark-induced 'turbulent spot' in its plane of symmetry. The three-dimensional description of the spot and its vorticity, streamline and Reynolds stress distributions as well as measurements for the cases of initially turbulent boundary layer and two spanwise spots will be presented later.

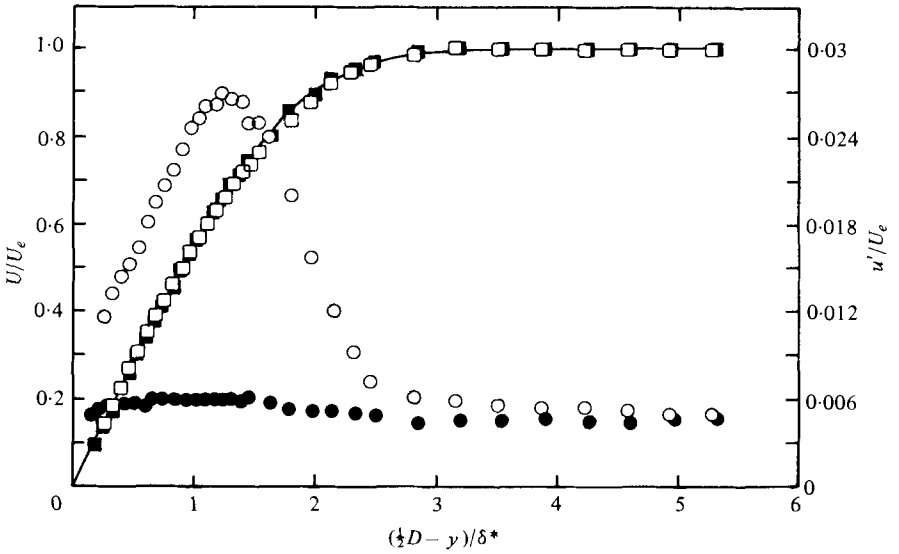

FIGURE 2. Initial mean velocity and fluctuation intensity profiles. □, U/U_e; ○, u'/U_e. Solid symbols without needles.

3.1. *Basic state*

Before discussing the spot dynamics, it is necessary to define the basic state of the flow in the absence of the spot. This description should include the initial condition as well as streamwise variation of the unperturbed flow geometry.

The characterization of the initial condition is indeed very critical since the near-field flow structure as well as its integral measures are strong functions of the initial condition (Bradshaw 1966; Foss 1977; Hussain & Zedan 1978*a*, *b*). In a jet with an initially laminar boundary layer, there are usually some significant fluctuations within the boundary layer, owing to unavoidable periodic thickening and thinning of the laminar boundary layer ascribed to settling-chamber cavity resonance modes (Hussain & Clark 1977), which are typically responsible for producing most of the exit centre-line fluctuation intensity. The fluctuation intensity profile within the boundary layer will have its peak noticeably away from the wall, typically at $y \simeq \delta^*$, and the spectra will consist of low, discrete frequencies. On the other hand, a trip ring may produce a separated shear layer which, though turbulent, may not reattach before exit as is typically assumed. In fact, because of this possibility (Brown & Roshko 1974; Batt 1975; Champagne *et al.* 1976; Chandrsuda *et al.* 1978) as well as strong dependence of the near-field on the initial condition, all near-field investigations of free shear flows should include careful documentation and calibration of the initial condition.

Figure 2 shows the initial mean velocity and longitudinal fluctuation intensity profiles 1 mm downstream from the lip with and without the needles in place, in the plane of symmetry. Note that the mean profile is unaffected by the presence of the needles and agrees very well with the Blasius profile. The corresponding displacement thickness δ^* and momentum thickness

$$\theta \equiv \int_0^\infty (U/U_e)(1 - U/U_e)\, dy$$

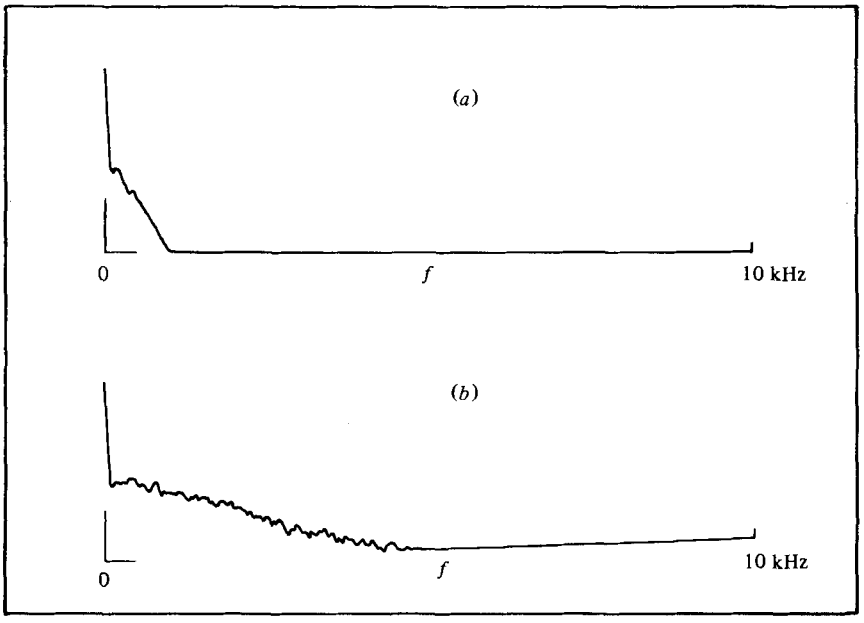

FIGURE 3. Initial u' spectrum: (*a*) without needles; (*b*) with needles. Frequency scale is linear; ordinate scale is logarithmic but arbitrary.

were 0·0113 cm and 0·0285 cm, respectively. The measured shape factor $\delta^*/\theta = 2{\cdot}52$ agrees well with the Blasius profile value 2·59. This difference may be because the measurements were made slightly downstream from the lip. The effect of the needles on the boundary-layer fluctuation intensity is striking. The fluctuation-intensity profile with its peak located at $y \simeq \delta^*$ is typical of initially laminar states of jets. Figure 3 shows that the spectral content of the velocity signal, predominantly below 150 Hz, is broadened by the presence of the needles; the frequency scale is linear and the (logarithmic) amplitude scale is arbitrary.

Figures 2 and 3 clearly demonstrate that the wakes of the two needle tips (1·4 cm apart) are in fact acting as transition wedges with a half-angle of about 6°, typical of the transitional spot, so that the two wedges presumably merge at the lip (6·8 cm downstream). The large peak longitudinal fluctuation intensity ($\simeq 3\,\%$) would tend to suggest that the flow is in an advanced state of transition. However, if this was so, the mean profile would also have undergone rather rapid change and thus produced an abrupt change in the shape factor (Schubauer & Klebanoff 1955). One can argue that the Reynolds stress history is too short to yet induce any noticeable change in the mean profile at the lip while the boundary layer is in a state of transition. From this viewpoint, if an ideally laminar initial boundary layer is desired, care should be taken to avoid completely any transition wedge. Note that the displacement thickness Reynolds number $U_e\delta^*/\nu$ at the exit is less than half the transitional value of approximately 950 (Schlichting 1968, p. 132).

The effect of the presence of the needles on the initial spot development is not clear. However, data taken at the azimuthal locations of 45°, 90°, 135° and 180° at $x/D = 1{\cdot}5$, 3·0 and 4·5 show that the phase-average spot coherent structure signatures are essentially the same as those presented herein (in the plane of symmetry of the

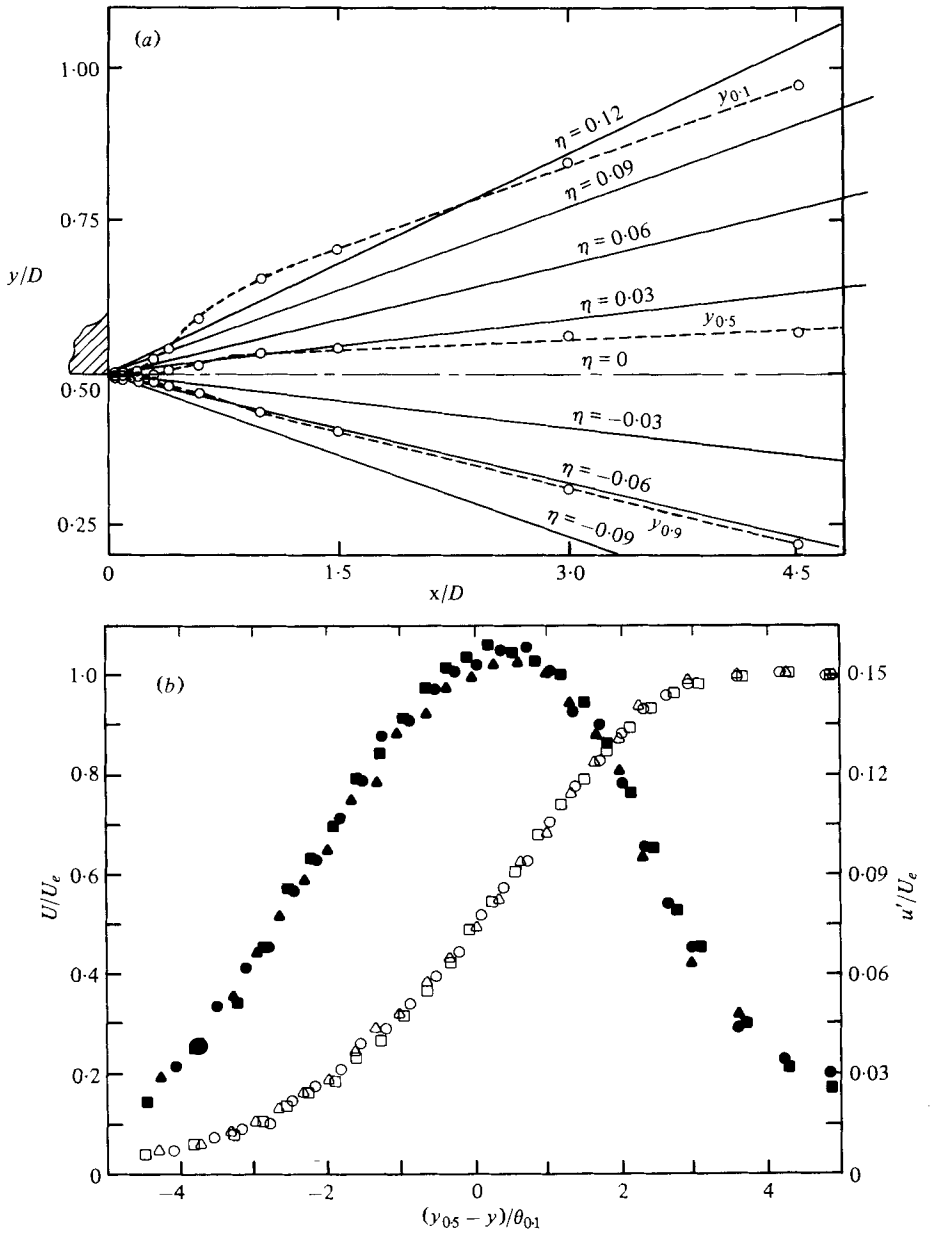

FIGURE 4. (*a*) Shear-layer boundaries and constant η lines. (*b*) Mean velocity and fluctuation intensity profiles at the three measurement stations. ○, ●, x/D = 1·5; □, ■, x/D = 3·0; △, ▲, x/D = 4·5.

needles). Similar eduction and phase-average measurements in the axisymmetric mixing layer in the plane of symmetry without the spark produced absolutely no structure. We can thus conclude that the overall effect of the presence of the needles on the shear-layer spot structure is inconsequential.

The boundaries of the mixing layer are depicted by the dotted lines marked by $y_{0\cdot1}$ and $y_{0\cdot9}$ in figure 4(*a*): these correspond to the transverse locations where the mean

Station	x/D	$\theta_{0\cdot1}$	δ_ω
1	1·5	0·255 cm	1·326 cm
2	3·0	0·497 cm	2·625 cm
3	4·5	0·725 cm	3·908 cm

TABLE 1

velocity is 10 % and 90 % of the maximum velocity. Also shown is the 50 % maximum-velocity line. Note that the time-dependent roll-up of the shear layer into toroidal vortex rings is evident even from the time-average boundaries at $x/D \simeq 0{\cdot}6$. Pictures of the visualization of axisymmetric mixing layer of a circular jet under controlled excitation (Hussain & Zaman 1978*a*) have shown the roll-up of the layer with the bulge on the low-speed side. Large fluctuation intensity and even flow reversal on the low-speed side associated with the roll-up contribute to the bulge in the $y_{0\cdot1}$ line, but it is likely to be a lesser contributor to the bulge in the $y_{0\cdot5}$ line. Also shown in this figure are lines of constant values of $\eta = (y - \frac{1}{2}D)/x$; in all subsequent figures η will be used as the transverse co-ordinate. Even though η = constant lines do not coincide with U/U_e = constant lines, the use of η as the transverse co-ordinate has facilitated easy control of the probe traverse and has essentially eliminated the effect of streamwise variation of the shear-layer width.

The use of η as the transverse co-ordinate requires an examination of the virtual origin x_0. The momentum and vorticity thicknesses $\theta_{0\cdot1}$ (defined later) and δ_ω measured at the three measurement stations are shown in table 1.

Linear extrapolations of $\theta_{0\cdot1}(x)$ and $\delta_\omega(x)$ produce the same virtual origin, i.e. $x_0 = -0{\cdot}13D$, which is consistent with the data of Hussain & Zedan (1978*a*) showing that the virtual origin is always located upstream from the lip for the initially laminar shear layer. If determined by extending the linear parts of $y_{0\cdot1}$ and $y_{0\cdot9}$, the virtual origin would be located further upstream. However, compared to $y_{0\cdot1}$ values, the integral measures $\theta_{0\cdot1}(x)$ and $\delta_\omega(x)$ are much more reliable and thus x_0 is taken to be $-0{\cdot}13D$ for the present experiment. Because of this small value, x_0 was ignored and, consistent with Bruun (1977), η was used as the transverse co-ordinate.

Detailed spot data have been taken at three x locations corresponding to $x/D = 1{\cdot}5$, 3 and 4·5 ($D = 12{\cdot}7$ cm). Note that, over the x range covering the three stations, the variation of the shear layer width is linear and the $y_{0\cdot1}$, $y_{0\cdot5}$, and $y_{0\cdot9}$ lines are almost parallel to the $\eta = 0{\cdot}09$, 0 and $-0{\cdot}06$ lines, respectively.

The mean velocity and turbulence intensity profiles at these three reference stations are shown in figure 4(*b*). The transverse co-ordinate is non-dimensionalized by an appropriate local length scale, viz.

$$\theta_{0\cdot1}(x) \equiv \int_{y_{0\cdot1}}^{\infty} (U/U_e)\,(1 - U/U_e)\,dy,$$

which is proportional to $(x - x_0)$ in the self-preserving region. In order to minimize the effects of large-turbulence intensity and transverse-entrainment velocity on the low-speed side, the integration is terminated at $U/U_e = 0{\cdot}1$. We have found that the mean-velocity and turbulence-intensity profiles are self-preserving for $x/D \gtrsim 1$ and that the shear-layer length scales $\theta_{0\cdot1}(x)$ and $\delta_\omega(x)$ vary linearly for $x/D \gtrsim 1$. The mean

velocity and turbulence intensity profiles at the three stations are congruent (figure 4*b*). The scatter in the u' data would be reduced if a longer averaging time were chosen. The value of the similarity parameter σ was 11·94, determined from the least-squares fit of the mean velocity data with the Tollmien profile (Abramovich 1963, p. 64); the peak turbulence intensity u'_p/U_e was about 0·16. Longitudinal one-dimensional frequency spectra, taken at a large number of x stations along the line corresponding to $U/U_e = 0{\cdot}8$, show that the spectral evolution is complete at $x \simeq 10$ cm (Husain & Hussain 1979). Thus, the evolutions of mean and turbulence profiles and u' spectra show that the three x stations chosen are in the (apparent) self-preserving region of the axisymmetric mixing layer. No effort has been made to correct the mean-velocity and turbulence-intensity profiles for large turbulence-intensity errors on the low-speed side of the mixing layer, as any correction scheme is questionable, unless removed by a biasing technique like the flying hot wire (Cantwell & Coles 1978, private communication). However, these errors are significant only in the potential flow part of the low-speed side (confirmed by a study in our laboratory of the simultaneous signal traces from a probe consisting of a cold wire located just upstream of a hot wire) and thus would not noticeably affect the coherent-structure phase-average measurements.

3.2. *Spot data acquisition and processing*

The data acquisition in this study was carried out with the help of our laboratory digital computer (HP 2100S). The sequence was as follows. The spot was initiated by a spark triggered by a function generator; the voltage pulse driving the spark served as a reference clock for delaying the signal digitization so that the recorded data sample (i.e. signal time series) captured the spot coherent-structure signature. The time delay necessary at each station was determined from a preliminary determination of the approximate convection velocity of the spot in the middle of the mixing layer and the streamwise separation between the spark and the probe location. After the preset delay, which was measured by a counter with $\pm$ 0·001 ms resolution, the 12-bit A/D converter was activated by the delay trigger, and 500 sequential data points spanning the spot signature were digitized at the rate of 8·4 kHz. At each location, data were recorded for 200 successive sparks. A fraction of this ensemble size was discarded on the basis of some signal enhancement criteria (discussed later). These digital data were recorded on magnetic discs. The operation was repeated for different transverse (radial) locations at the three x stations. The same hot wires were used for all the measurements. The data were subsequently processed on the minicomputer.

The spot-induced motion has been educed by phase averaging over about 200 optimally aligned signal traces. Because the choice of a particular eduction process depends on the type of information of interest and because the eduction results depend upon the process involved, a careful documentation of the eduction technique is required. The goal of this investigation was to educe the 'average' signature of the spark-induced spot. It must be recognized that, owing to the large-intensity velocity fluctuations in a mixing layer, the spot structure in the mixing layer is relatively weak. Thus, the eduction of the signal in the mixing layer is a much more difficult task than that in the boundary layer.

Since the random fluctuations cancel out in the averaging process, the phase-sensitive ensemble average sifts out the underlying coherent structure buried in a random signal

(Hussain & Reynolds 1970). Owing to the turbulent nature of the spot and its surrounding flow, the evolution of a spot in a turbulent mixing layer is marked by various kinds of distortions. For an observer moving with the spot, there will be observable distortions in the spot shape, size and orientation, whereas a stationary observer will also detect a variation in the spot arrival time due to the mixing-layer turbulence-induced jitter in the convection velocity. Clearly, a straightforward ensemble average of the time-referenced signal realizations will tend to smear out the spot boundary as well as its distinguishing features. For a stationary observer, a complete description of the spot requires a four-dimensional probability-density surface. Every point on this surface will represent a certain shape, size, orientation and arrival time – which can be achieved by a multisensor probe where the orientations of the sensors can be adjusted to lock on a given size and shape of the structure. The primary thrust of this study was to educe an average size and shape of the spot structure, and, thus, the signal eduction technique focused only on the elimination of the jitter in the spot arrival time. It must be mentioned that the jitter, which is caused by interaction between the spot and the surrounding turbulent flow, is at the heart of the flow physics. However, in order to educe the average characteristics of the spot, it is necessary to eliminate the arrival-time jitter.

The alignment procedure will be simple if there is a unique feature of the signal, such as an abrupt jump or spike in any property associated with the spot, to use as a reference. However, the large-amplitude random velocity fluctuations, especially in a mixing layer, will totally overshadow the signal. Therefore, for the turbulent mixing layer, there is no dominant local criterion to align the time signals based on any feature of the signal itself. It was thus decided to obtain an overall alignment of the individual signals based on some global criterion. The underlying concept is that, since only the spot signature, even though totally submerged in turbulent velocity fluctuations, is the common aspect of two signal traces, these traces will produce maximum cross-correlation when the spot signatures are aligned. Thus maximum correlation between two signal traces is an indication of the alignment of the spot signatures.

The key step was to educe an average signature of the spot, and then successively iterate on the average signature until a final signature was converged upon. It should be apparent that if the coherent structure signature has a characteristic, albeit hidden, feature, such an iteration process should be convergent. A straightforward ensemble average of all realizations gave the initial guess (zeroth iteration) of the spot signature. Each realization was then individually cross-correlated with this average to determine the time shift τ_s and a new ensemble average of these shifted realizations was obtained. This gave the second iteration of the spot coherent-structure signature. The process was repeated until convergence was achieved. In order to accelerate the convergence as well as to assure that the large-scale coherent-structure signature of the spot was emphasized in cross-correlation, the raw signals were digitally low-pass filtered (at 500 Hz) before the alignment process started. Since the 'spot' is assumed to be a large-scale entity, the filtering was intended to retain the structure information but eliminate accidental alignment with a large-amplitude random fluctuation (of high frequency) and thus accelerate the alignment process. The technique is somewhat similar to that used by Zilberman *et al.* (1977) in the boundary-layer spot study, except that they obtained the cross-correlation through FFT.

The alignment approach is quite different from that employed by Lau & Fisher

(1975) and Bruun (1977) in the detection of naturally occurring coherent vortex structures in the axisymmetric mixing layer. Lau & Fisher educed the coherent structure signal based on the positive and negative spikes in the u signals, these spikes representing the front and back sides of the structure, respectively. Bruun, however, has shown that this approach produces distinctly different values of the coherent-structure characteristics and the convection velocity, depending on whether positive or negative signal peaks are used for detection. He also demonstrated improved structure detection when triggering is based only on the high peaks of the spikes. Lau & Fisher and Bruun used an eduction method where the eduction was triggered by a prescribed feature (i.e. spike) of the structure signature. Bruun based his eduction on the large peaks only. His results are, thus, biased towards a subclass (i.e. the strongest) of the coherent structures. In the alignment technique employed here there is no such bias. The initiation of a spot at a known time and its detection at a prescribed location and subsequent signal alignment through cross-correlation to reduce variations in the arrival time should produce an average coherent structure representative of the spot.

The convergence of the ensemble average was concluded when the signal enhancement reached the maximum possible, i.e. when any further alignment would produce no noticeable improvement of the correlation. Operationally, this was effected by specifying a minimum allowable shift. That is, if at any stage of iteration all required time shifts indicated by cross-correlation fell below a set time delay the iteration was terminated. The minimum time shift permitted ranged from 0·24 ms to 0·60 ms; this criterion was relaxed within these arbitrary limits when the number of iterations necessary for optimum alignment increased. This was done in order to save computation time on the low-speed side where the signal is influenced by relatively large-amplitude random fluctuations which introduce large jitters in the arrival time. This relaxation is of no consequence to the final results since the estimated maximum uncertainty in the ensemble-average velocity is less than 2 %. (The convergence criteria were checked through computer study of synthetic signals of known features, viz. square and triangular waveforms; convergence in these cases was always achieved after the first iteration.) The number of iterations required varied from 2 to 20, the high-speed side requiring the lowest number of iterations and the low-speed side the largest.

An additional step was undertaken to sharpen the signal-enhancement process; this involved rejection of 'bad' realizations. A maximum allowable total time shift was determined by computing the standard deviation (σ) of the time shifts in the first iteration. From the record of cumulative time shifts, those realizations requiring time shifts above 3σ were considered 'bad' and thus were rejected so that the ensemble average involved those with 'purer' signatures. The rationale for this procedure is that the rejected signal realizations have excessive arrival-time jitter, and thus have been subjected to unusual turbulence activity and interaction and, consequently, have undergone excessive distortions and decay or breakdown.

In order to elucidate the data acquisition and analysis process, as well as simultaneously to focus on some physics of the flow, data are presented at three transverse locations for each of the three stations. These locations emphasize the inherently different flow structure on the high-speed, middle, and low-speed sides of the mixing layer as well as depict the streamwise evolution of the structure.

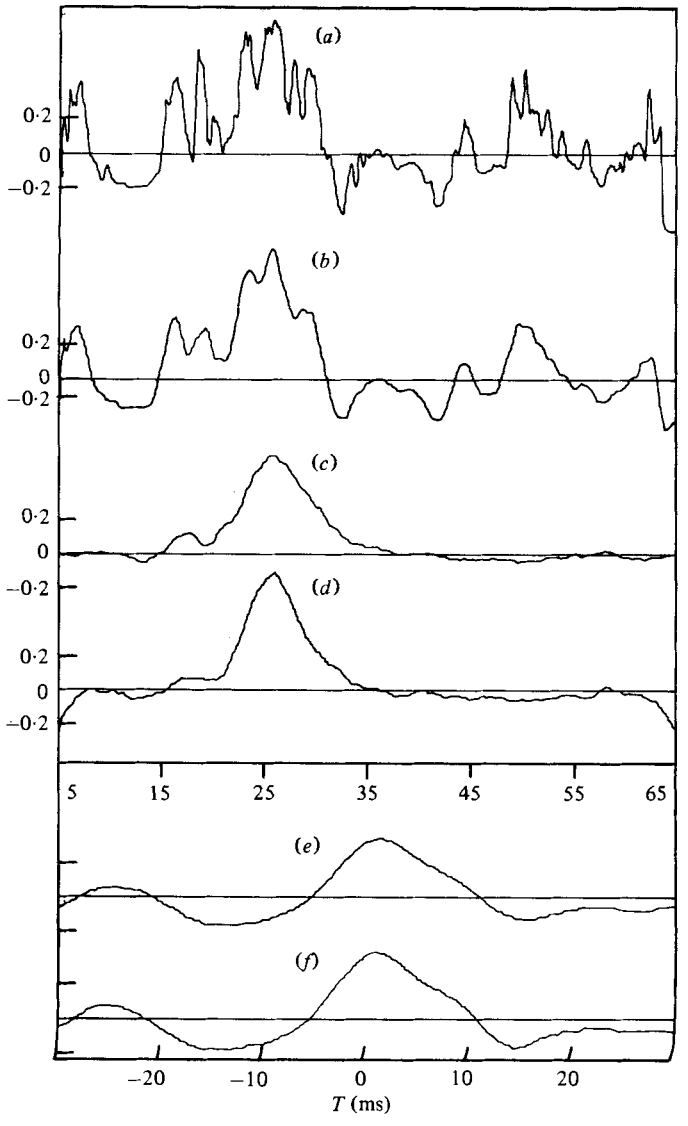

FIGURE 5. Signal eduction at $x/D = 1{\cdot}5$, $\eta = 0{\cdot}09$. (*a*) One realization of the raw $\tilde{u}(t)/U_e$ signal; (*b*) filtered $u_f(t)/U_e$; (*c*) zeroth-iteration ensemble average of $u_p(t)/U_e$; (*d*) final iteration ensemble average of $u_p(t)/U_e$; (*e*) cross-correlation between (*b*) and (*c*); (*f*) cross-correlation between (*b*) and (*d*).

For $x/D = 1{\cdot}5$, the application of the signal enhancement technique at $\eta = 0{\cdot}09$, $0{\cdot}03$ and $-0{\cdot}06$ are illustrated in figures 5, 6 and 7, respectively. The corresponding data for $x/D = 3{\cdot}0$ are shown in figures 8–10 and for $x/D = 4{\cdot}5$ in figures 11–13.

Figure 5(*a*) shows the instantaneous longitudinal velocity trace $\tilde{u}(t)/U_e$ at the location $\eta = 0{\cdot}09$, the mean velocity U/U_e at this location being $0{\cdot}24$. The ordinates in traces (*a*)–(*d*) of this and other similar figures (6–13) denote the phase-average longitudinal velocity $u_p(t)$ divided by the mixing-layer characteristic velocity U_e. The local time-average $\overline{U}$ at each location has been subtracted from the time traces so that the

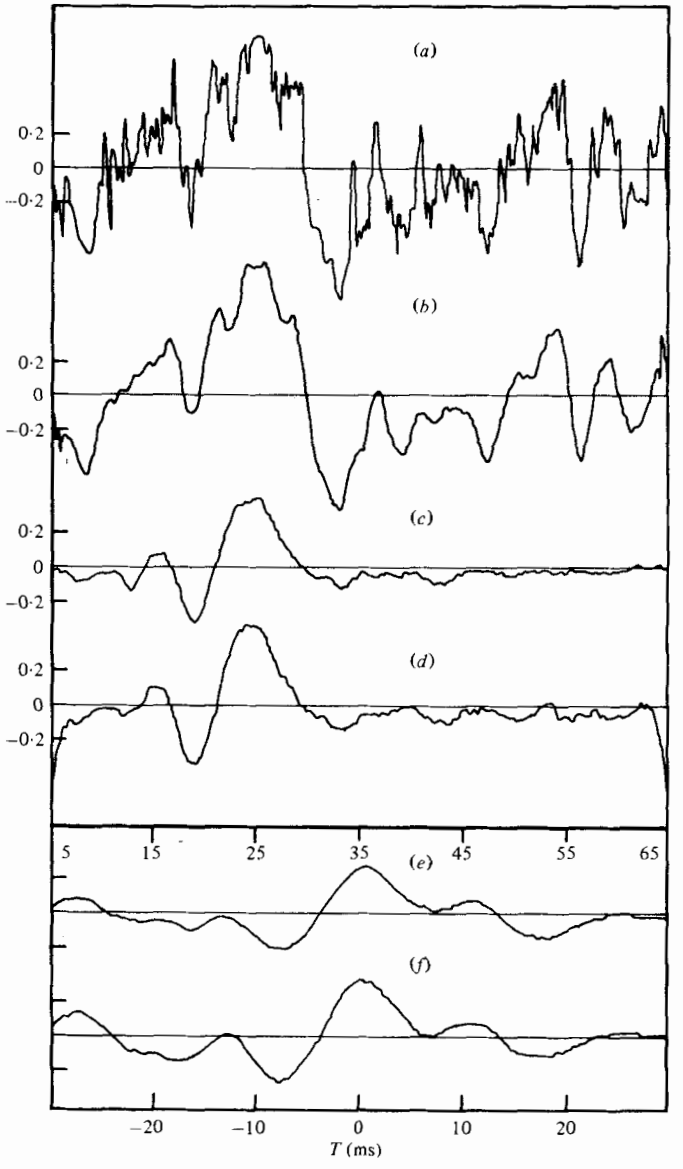

FIGURE 6. Eduction at $x/D = 1{\cdot}5$, $\eta = 0{\cdot}03$; for legend on traces (*a*)–(*f*) see figure 5.

details of the spot signature can be highlighted. Figure 5(*b*) shows the corresponding filtered signal $u_f(t)$, where the high-frequency spikes associated with the background turbulence have been diminished. The spot coherent-structure signature, expected to be of low frequency, is retained in the filtered signal. The number of iterations required to align the signals and obtain the coherent-structure signature can be significantly reduced by pre-low passing the signals through a filter. Furthermore, the number of realizations required for convergence is reduced. This is a significant saving in computer analysis time.

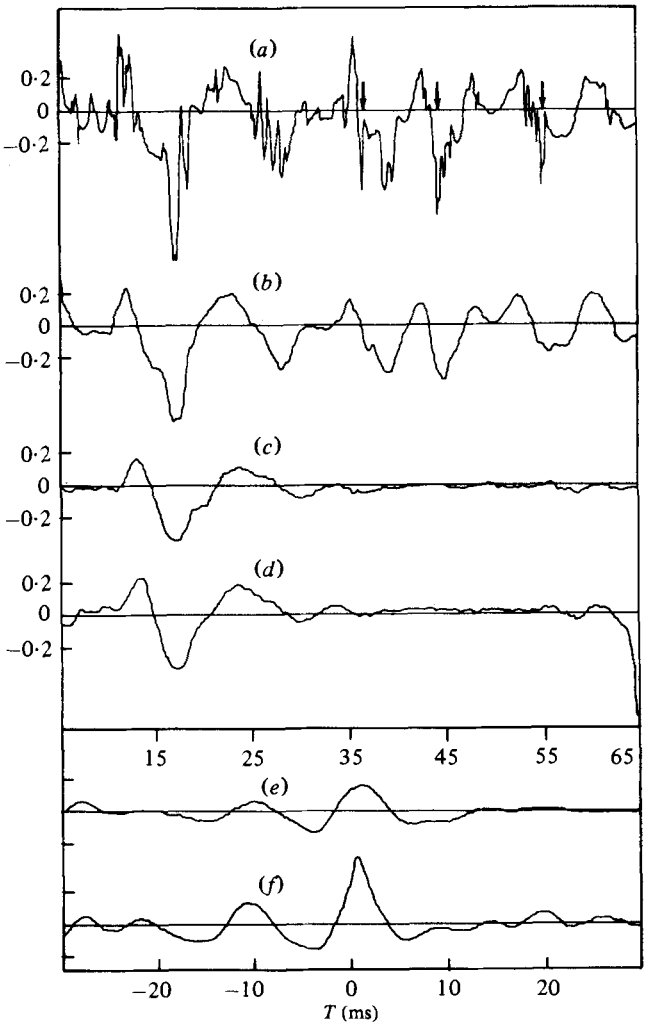

FIGURE 7. Eduction at $x/D = 1{\cdot}5$, $\eta = -0{\cdot}06$; for legend on traces (*a*)–(*f*) see figure 5.

Figure 5(*c*) shows the ensemble average (zeroth iteration) of 200 realizations of the filtered signal. Note that the large undulations on the right-hand side of the filtered trace do not appear in the ensemble average. These undulations may be signatures of naturally occurring structures, but contribute nothing to the ensemble average because they occur randomly in space and time. It is impressive that even the first iteration has captured a distinctive signature of the spot.

Figure 5(*e*) shows the cross-correlation between traces (*b*) and (*c*). Figure 5(*d*) shows the final-iteration ensemble-average velocity trace $u_p(t)$, and figure 5(*f*) is the cross-correlation between traces (*b*) and (*d*). The corresponding traces for the two other transverse locations at $x/D = 1{\cdot}5$, and for $x/D = 3{\cdot}0$ and $4{\cdot}5$ are shown in the figures 6–13. The ordinate scales in correlation traces (*e*) and (*f*) of figures 5–13 are linear but arbitrary.

A number of interesting features of the spot signature and the relevance of the 'spot'

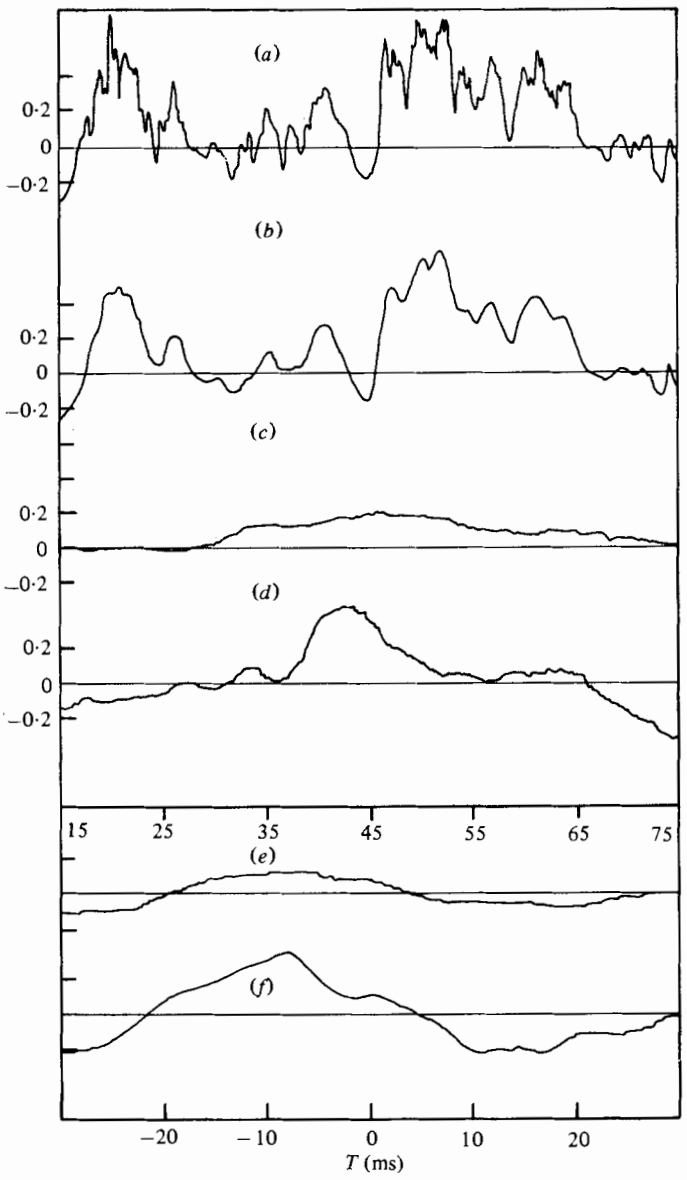

FIGURE 8. Eduction at $x/D = 3{\cdot}0$, $\eta = 0{\cdot}09$; for legend on traces (*a*)–(*f*) see figure 5.

to the naturally occurring coherent structures in the axisymmetric mixing layer can be inferred from figures 5–13. At the first station, the coherent structure signature is essentially similar before and after the alignment (traces (*c*) and (*d*)); consequently, the improvement in the cross-correlation (from trace (*e*) to (*f*)) is marginal. The same is not the case in the second and third stations. These traces suggest that the 'spot' is a relatively simple structure at station 1, but, as it proceeds downstream, it is subjected to the mixing-layer turbulence activity for longer times and thus undergoes larger distortions and jitter in the arrival times. The loss of coherence on the low-speed side will be much larger than on the high-speed side. The degradation of the

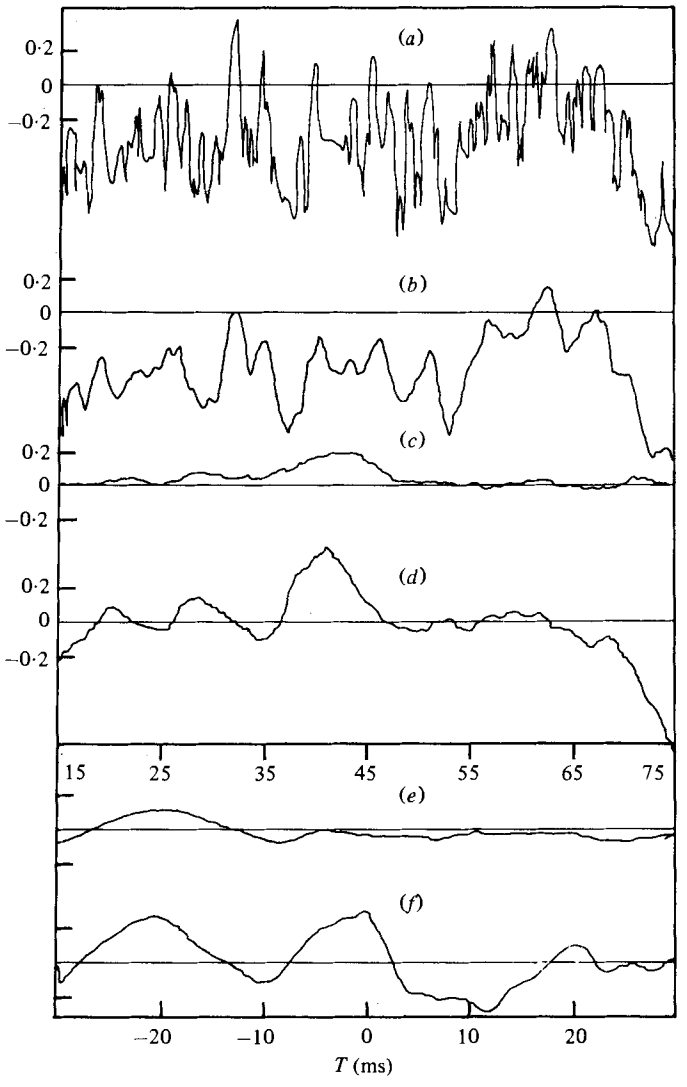

FIGURE 9. Eduction at $x/D = 3{\cdot}0$, $\eta = 0{\cdot}03$; for legend on traces (*a*)–(*f*) see figure 5.

zeroth-iteration (unaligned) ensemble average with increasing x will be the minimum on the high-speed side (compare traces (*c*) and (*d*) in figures 7, 10, 13) and the maximum on the low-speed side (compare traces (*c*) and (*d*) in figures 5, 8, 11). Because of increasing jitter in the arrival time, the effect of the signature alignment is more pronounced at later x stations; note the improvement in the ensemble average due to signal enhancement from trace (*c*) to trace (*d*) in figures 11 and 12. The cross-correlation traces (*f*) in the figures 7, 10 and 13 are sharper (with higher peaks) than the corresponding traces (*e*), as compared to the other figures.

Figure 14 shows the histograms of the total time shifts (in ms) required for convergence. The histograms (*a*) to (*i*) correspond sequentially to the cases shown in figures 5–13, respectively; the peak value in each histogram is indicated. Note that the

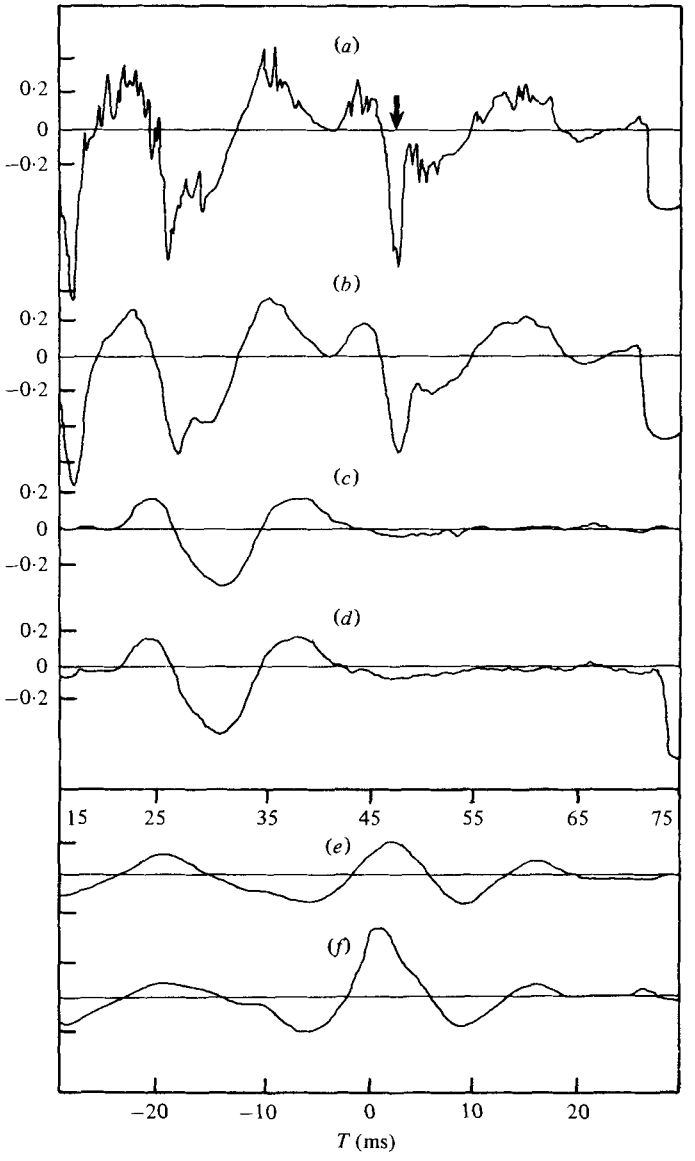

FIGURE 10. Eduction at $x/D = 3{\cdot}0$, $\eta = -0{\cdot}06$; for legend on traces (*a*)–(*f*) see figure 5.

standard deviation σ of the time-shift histogram is much smaller on the high-speed side compared to that in the middle of the mixing layer. Figure 14 shows that the loss of coherence is much more dramatic in the radial direction than in the flow direction, an observation consistent with the hot-wire and flow-visualization studies of the naturally occurring coherent structures in the axisymmetric mixing layer (Clark 1979). Figure 15 presents the transverse variations of the acceptance ratio, i.e. the fraction of the realizations finally accepted based on the alignment time shift criterion. This figure is included because it reflects the extent of signal jitter undergone by the spot at

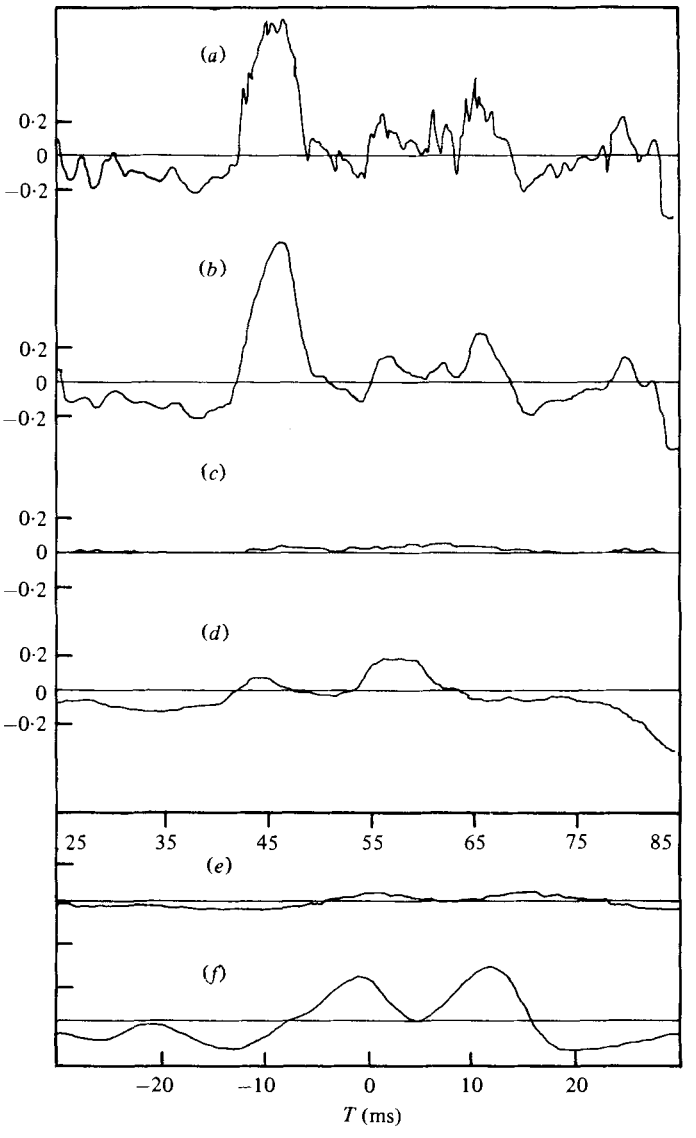

FIGURE 11. Eduction at $x/D = 4{\cdot}5$, $\eta = 0{\cdot}09$; for legend on traces (*a*)–(*f*) see figure 5.

different transverse (η) locations and, consequently, the extent of distortions of the spot at different η.

The observations of figures 5–15 may be summarized as follows: there is an increase in the standard deviation σ of time shifts required for alignment and a corresponding degradation of the zeroth correlation and acceptance ratio with both increasing η and streamwise location. Although the streamwise increase in σ is expected because of the corresponding increase in convection time of the spot, the transverse variation of σ is surprising. There is an apparently large variation of orientation of the spot, with the high-speed side being very repeatable in time while the low-speed side exhibits large variations from the average position for individual realizations.

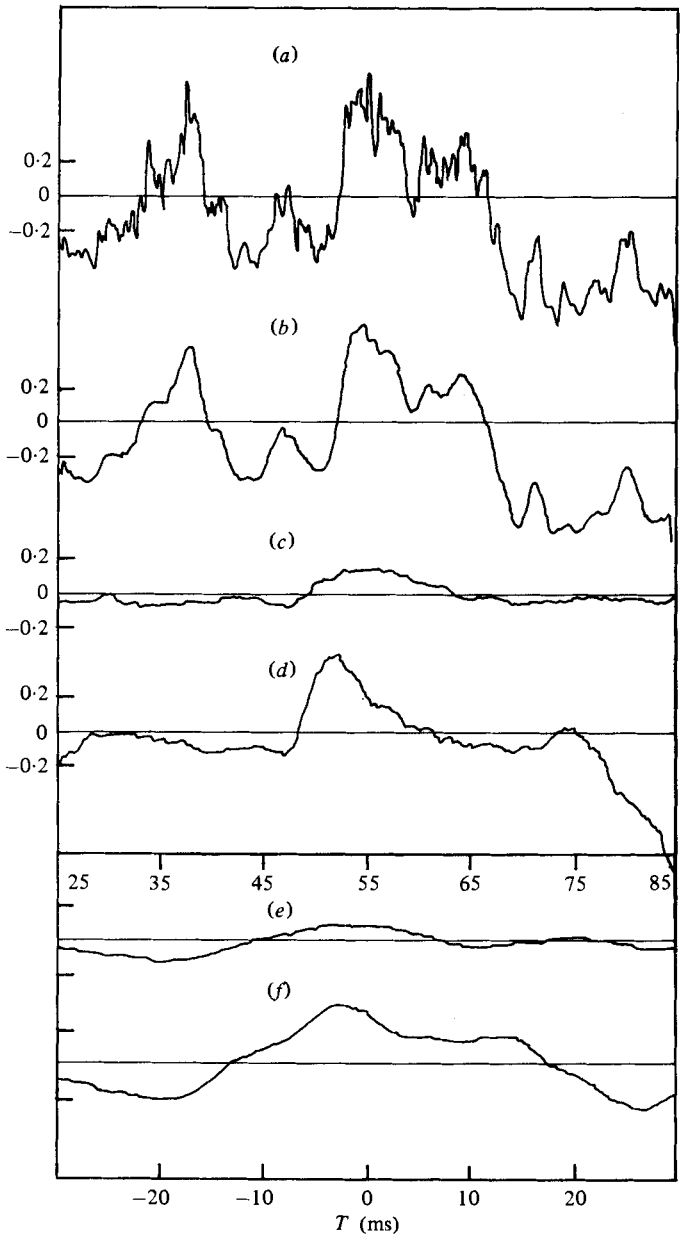

FIGURE 12. Eduction at $x/D = 4{\cdot}5$, $\eta = 0{\cdot}03$; for legend on traces (*a*)–(*f*) see figure 5.

3.3. *Signal interpretation*

In addition to depicting the signal-enhancement process, figures 5–13 also depict some interesting aspects of the flow. The mixing layer contains large-scale coherent vortical structures which perform most of the mixing. This would mean that each vortical structure transports high-momentum fluid from the high-speed side to the low-speed side of the shear layer at the front (downstream side) of the vortex and lower-momen-

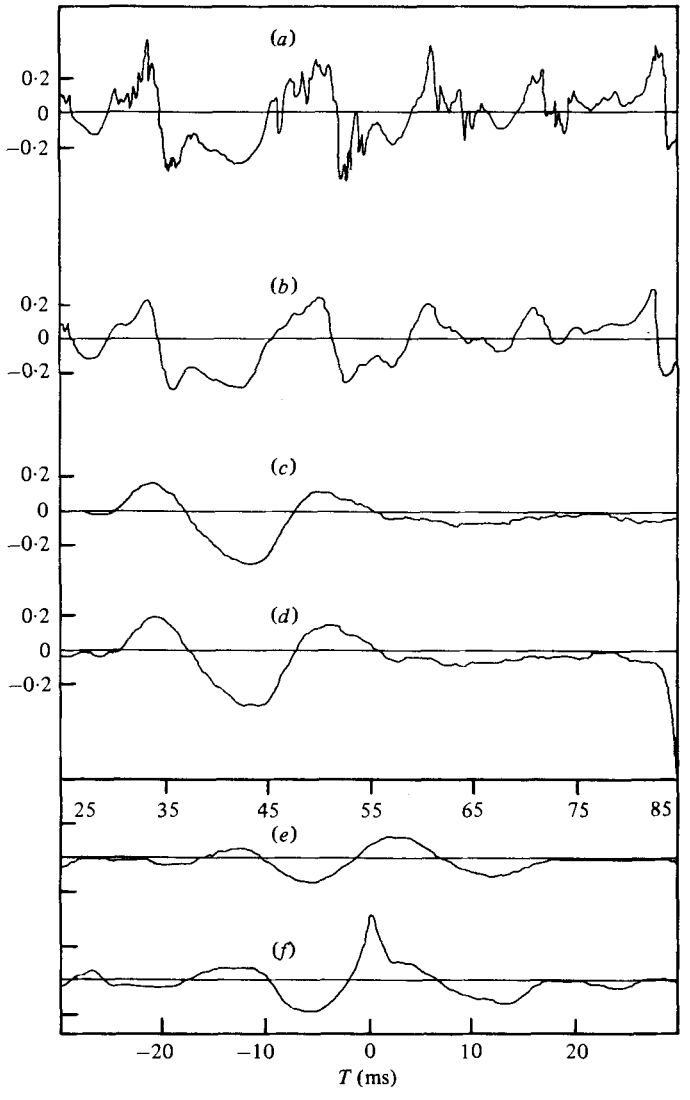

FIGURE 13. Eduction at $x/D = 4{\cdot}5$, $\eta = -0{\cdot}06$; for legend on traces (*a*)–(*f*) see figure 5.

tum fluid from the low-speed side to the high-speed side of the layer at the back of the vortex. Thus a hot-wire signal would contain isolated positive peaks on the low-speed side and negative peaks on the high-speed side.

The three negative peaks on the right-hand side of the trace in figure 7 (*a*) (marked by arrows) are not associated with the spot; the ensemble average contains no contribution from these because they occur in a mixing layer in a random manner. Note that the negative spike marked by an arrow in the high-speed side trace at station 2 [figure 10 (*a*)] also cannot be ascribed to a spot structure effect. The corresponding trace at station 3 [figure 13 (*a*)] does not show any clear negative spike at this location at the end of the potential core. It is also likely that the strong spanwise coherence of the spot structure in the axisymmetric mixing layer is broken down by the time the

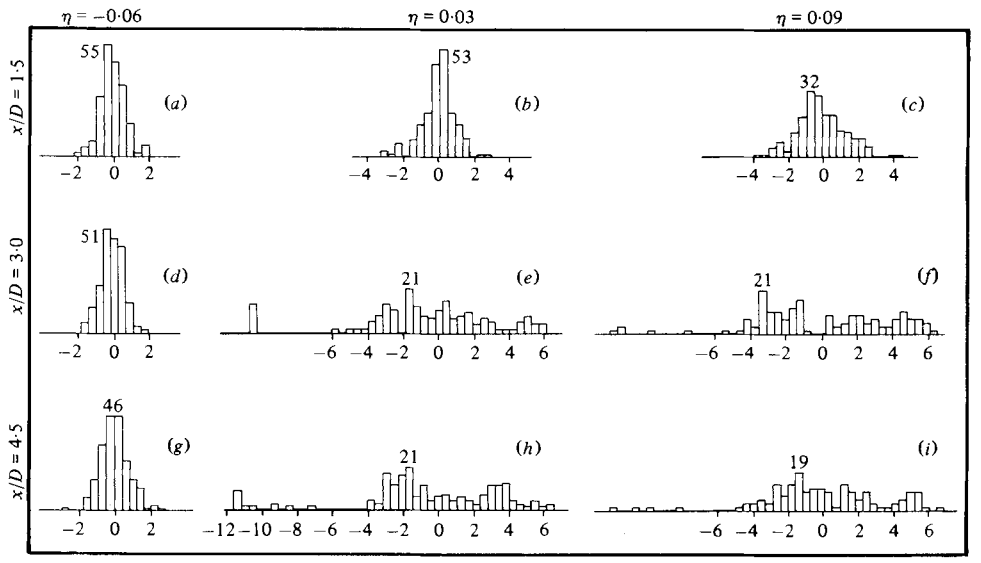

FIGURE 14. Histograms of time shifts of final alignment. Abscissa in milliseconds. Histogram peak values are indicated. Histograms (*a*) to (*i*) correspond sequentially to the cases shown in figures 5 to 13.

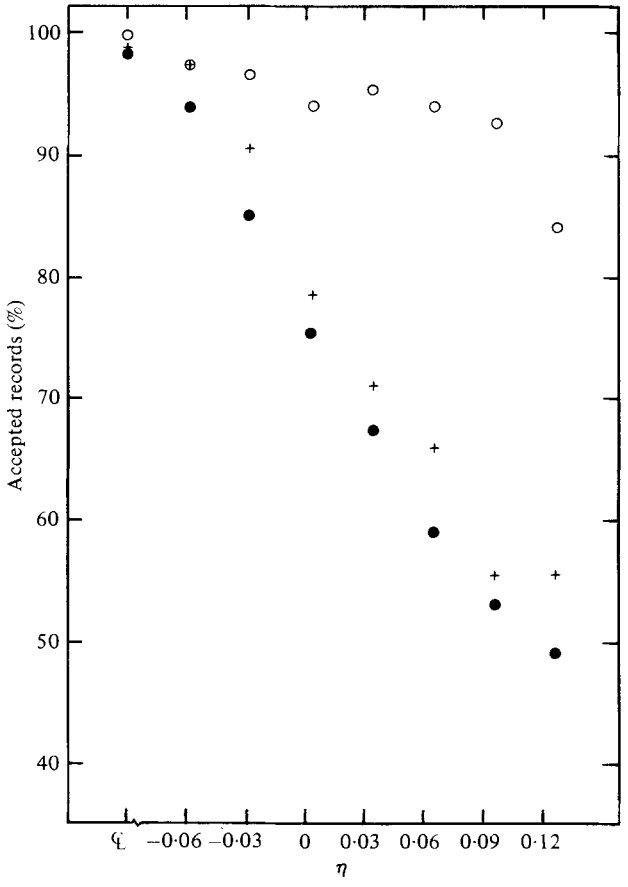

FIGURE 15. Acceptance ratio distributions; ○, $x/D = 1{\cdot}5$; +, $x/D = 3{\cdot}0$; ●, $x/D = 4{\cdot}5$.

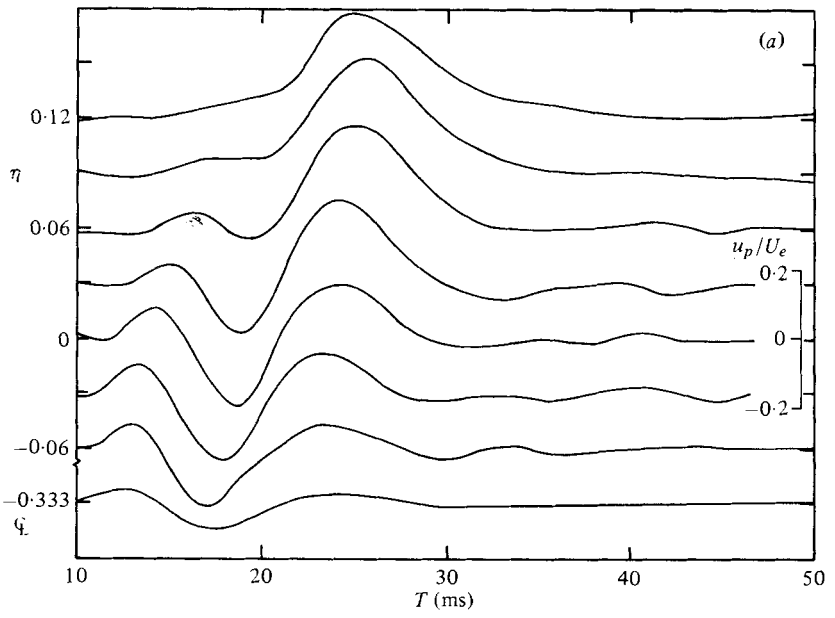

FIGURE 16 (*a*). For legend see page 88.

structure arrives at this location through evolution of strong three-dimensionality (Yule 1977; Davies & Baxter 1978; Zaman 1978).

The signal of a hot wire located at the centre-height of a vortex train will contain both positive and negative spikes and the frequency of occurrence of these peaks will be much larger depending on the number of vortex sheets in each vortex crossed by the probe. That is why figure 9 (*a*) has many more oscillations than figure 10 (*a*). Note that the smooth parts of the signals in figures 7 (*a*) and 10 (*a*) are due to the high-speed side potential flow and as such are absent in figures 6 (*a*) and 9 (*a*). On the low-speed side, the signal should contain positive peaks but cannot be clearly identified presumably because the signal is not very clean (owing to large fluctuation intensities).

3.4. *Spot structure*

Figure 16 (*a*) shows the composite of the final iteration ensemble-average longitudinal-velocity signal traces u_p at the first station as a function of the time delay T (ms) with respect to the spark trigger. The traces are staggered in η, marked on the left-hand boundary, the one with the largest η being at the top and the jet centre-line at the bottom. These time traces represent the ensemble-average variation from the local time mean. Figures 16 (*b*) and 16 (*c*) show the corresponding staggered profiles for stations 2 and 3, respectively. It is impressive that the spot signature is so clearly captured in these figures. At station 1, the spot extends across the entire mixing layer with marginal distortion of the shape due to shear. There is noticeable, albeit uncomplicated, distortion by the time the spot reaches 4·5 diameters downstream. Note that the jet centre-line trace at station 1 is much weaker than at stations 2 and 3 because the centre-line footprint of the spot is weaker at station 1, where the spot is smaller and farther from the jet centre-line.

To enhance the spot dynamics and its evolution, constant u_p contours have been

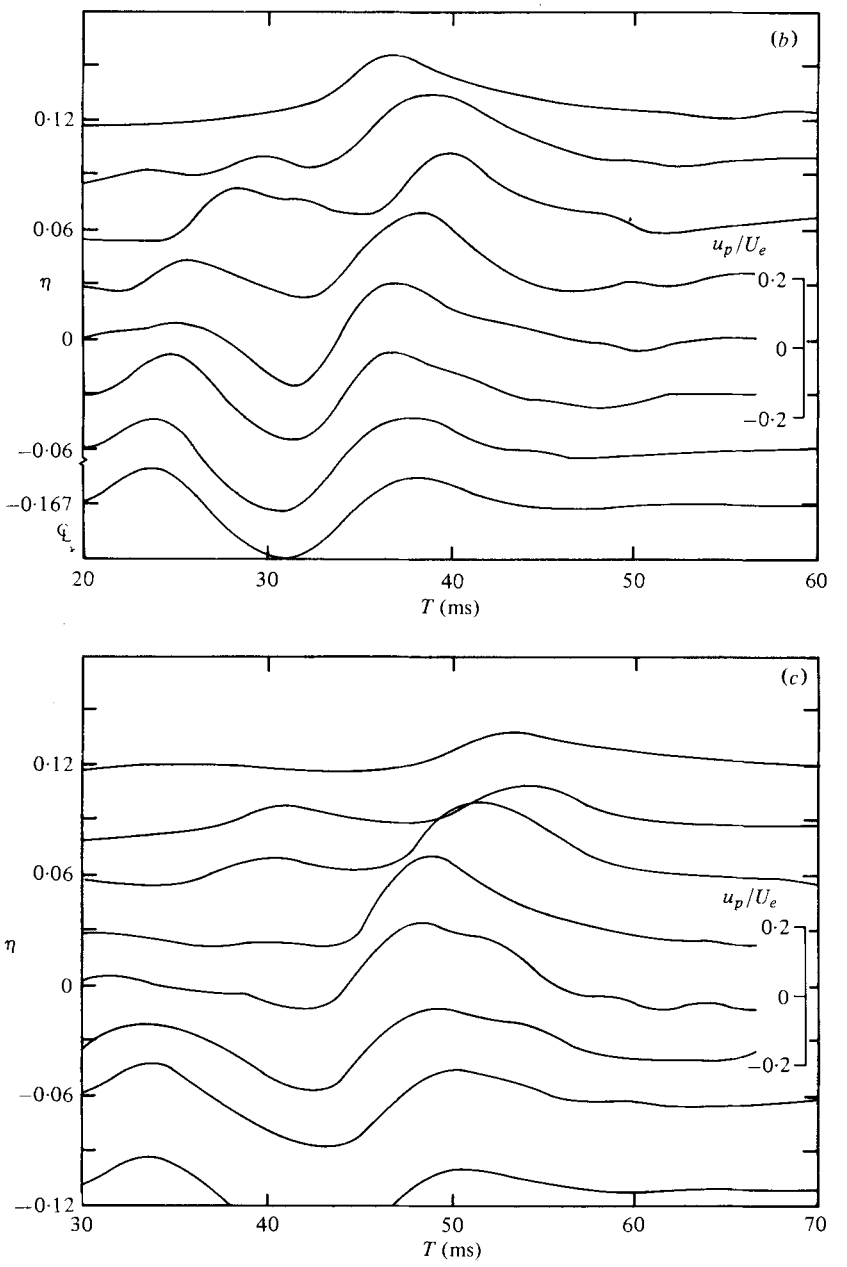

FIGURE 16. Staggered distributions of the final-iteration ensemble average $u_p(T)/U_e$. (*a*) $x/D = 1{\cdot}5$; (*b*) $x/D = 3{\cdot}0$; (*c*) $x/D = 4{\cdot}5$. With decreasing order from the top, the traces correspond to η values 0·12, 0·09, 0·06, 0·03, 0·0, −0·03, −0·06, marked on the left-hand side; the lowest trace is for the centre-line.

plotted in figures 17 (*a*), (*b*) and (*c*) corresponding to the stations 1, 2, and 3, respectively. The solid lines denote the regions of excess velocity perturbation due to the spot coherent structure and the dotted lines, the negative perturbation velocity regions.

The corresponding phase-averaged background (i.e. random velocity component)

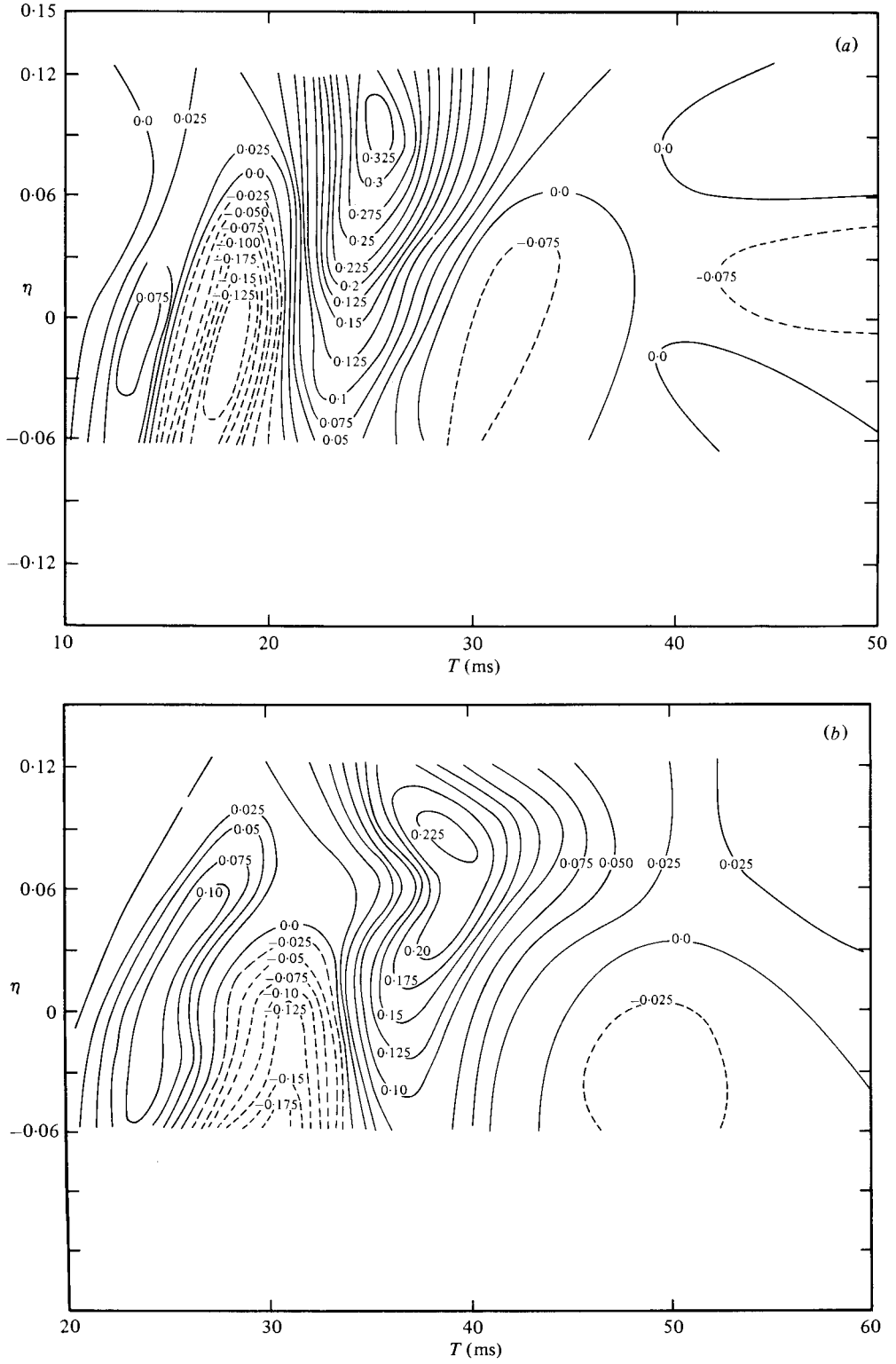

FIGURE 17 (*a*, *b*). For legend see page 90.

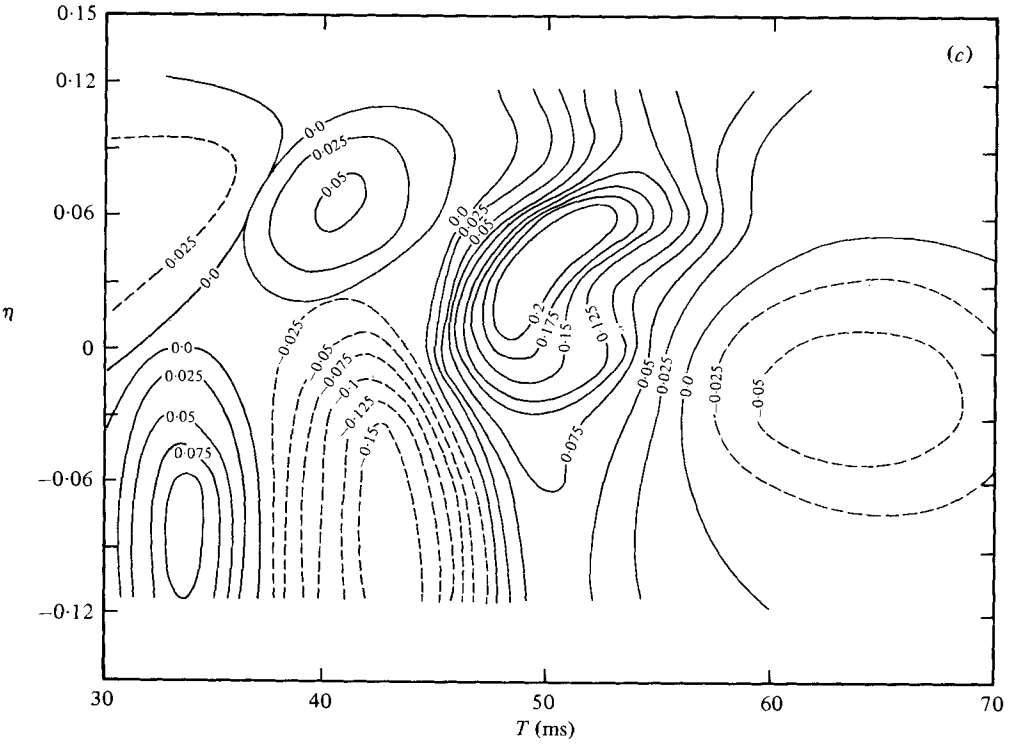

FIGURE 17. Constant u_p/U_e contours: (*a*) $x/D = 1{\cdot}5$; (*b*) $x/D = 3{\cdot}0$; (*c*) $x/D = 4{\cdot}5$.

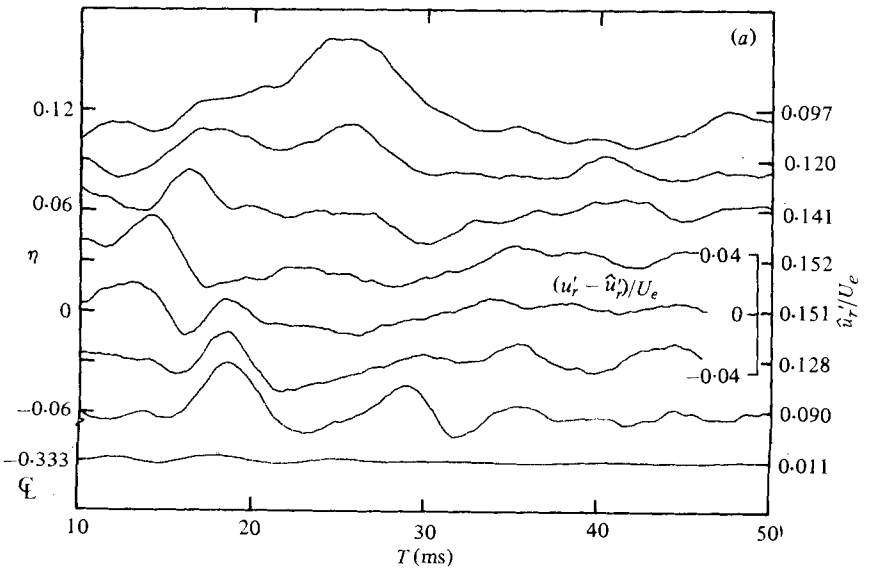

FIGURE 18 (*a*). For legend see page 91.

r.m.s. intensity staggered profiles are shown in figure 18 (*a*), (*b*) and (*c*) for stations 1, 2 and 3, respectively. The passage of the spot clearly corresponds to large-turbulence production. Note that large fluctuations occur typically on the low-speed side. However, a caution is in order when interpreting u_r' data. Even though the jitter in arrival

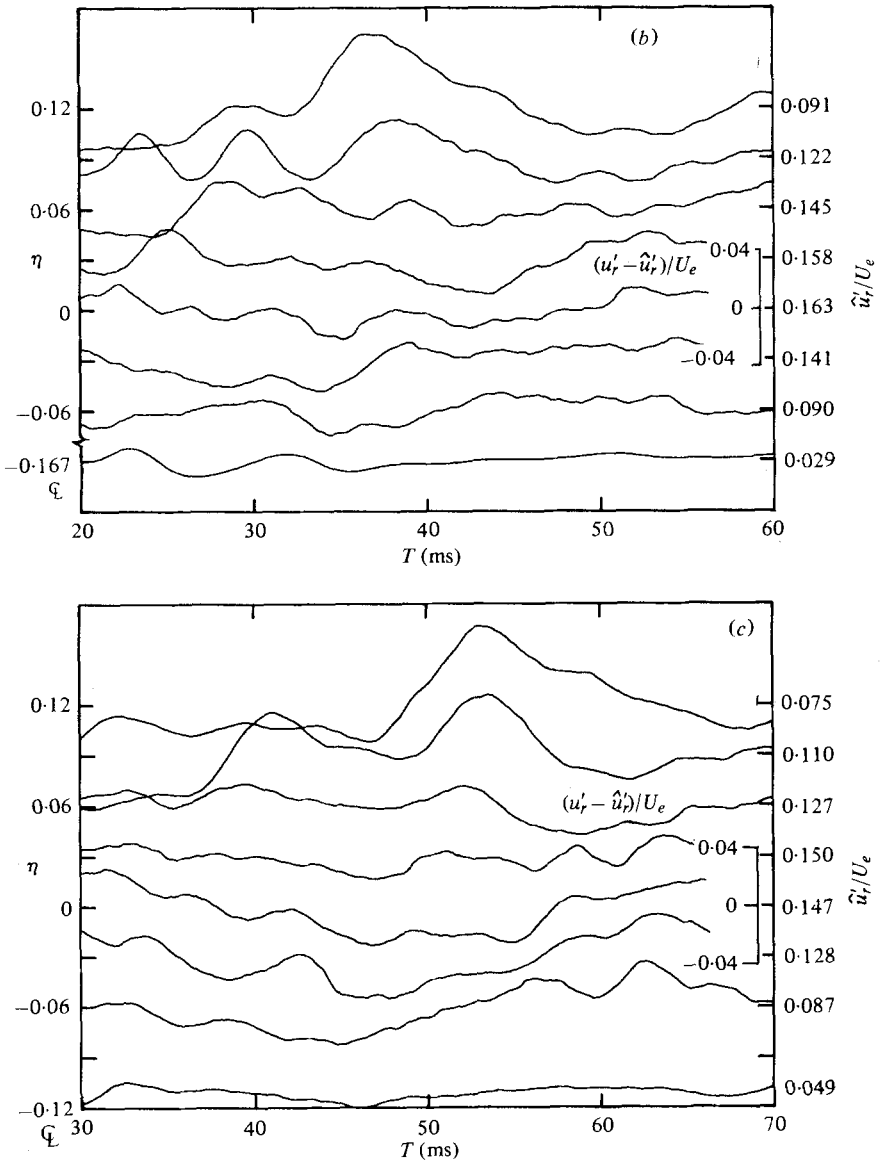

FIGURE 18. Staggered distributions of the longitudinal r.m.s. fluctuation intensity: (*a*) $x/D = 1{\cdot}5$; (*b*) $x/D = 3{\cdot}0$; (*c*) $x/D = 4{\cdot}5$. $\hat{u}'_r$ is the time average of u'_r over the trace length. For identification of the traces see figure 16 caption.

times has been eliminated through signal alignment, the jitter in the shapes and the sizes cannot be eliminated. These shape and size jitters themselves would contribute to the measured background-turbulence intensity as an artifact of measurement. The measured background-turbulence intensity will also be high at locations where the gradient of the phase-average velocity is the largest. In spite of all the drawbacks and unavoidable errors involved in u'_r computation, it is very encouraging to find that the zone average $\hat{u}'_r$ of u'_r (time average of the ensemble average) is extremely close (typical

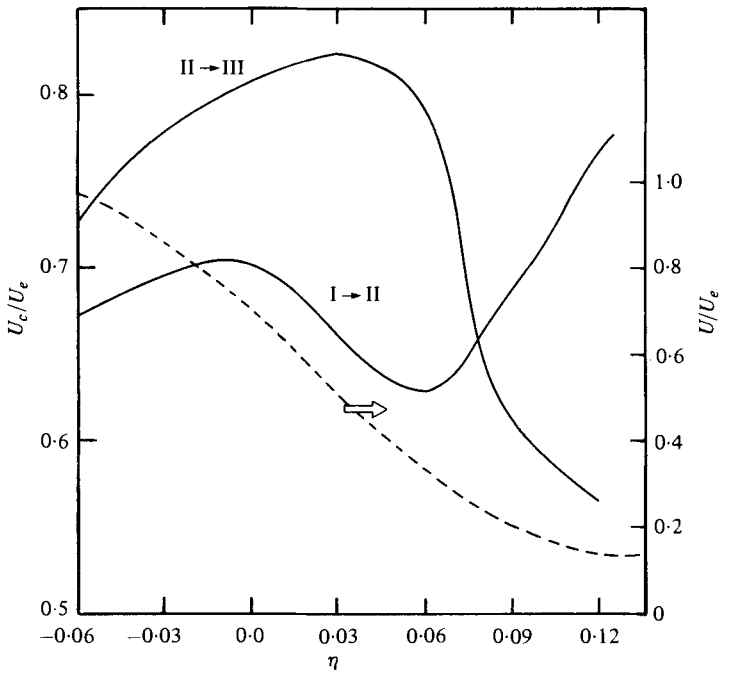

FIGURE 19. Convection velocity variation across the shear layer. I → II, between stations 1 and 2; II → III, between stations 2 and 3.

deviation 5 %) to the local time-mean turbulence-intensity value. Note also that the u_r' signature is much clearer in the low-speed side where the flow is more intermittent and most of the contributions to u_r' can be associated with the spot itself.

By identifying the characteristic features of the spot signature in the time traces in figures 16(*a*), (*b*) and (*c*), and noting the time differences between their occurrences in stations 1, 2 and 3, it is possible to determine a convection velocity U_c at each η. It is to be recognized that η = constant lines are not time-mean streamlines. This, together with the fact that the spot does undergo significant distortions during its travel from station 1 to 3 (Clark 1979), would suggest that these convection velocities are neither extremely precise nor clearly physically meaningful, but give an overall measure of the translation velocity of the spot. Figure 19 shows the average convection-velocity distribution across the shear layer. Note that the average of the convection-velocity profile between stations 1 and 2 is not significantly different from that between 2 and 3 even though the U_c profiles are quite different. The average convection velocity based on the centre of velocity-contour cells in figure 17 is $0{\cdot}71U_e$ between stations 1 and 2 and $0{\cdot}87U_e$ between stations 2 and 3.

Between stations 1 and 2 the convection-velocity profile is interesting; it is low on the jet centre-line, reaches a peak value at $U/U_e \simeq 0{\cdot}70$, a minimum at $U/U_e \simeq 0{\cdot}35$, and then increases again farther outside. Such a variation is not unreasonable in general. On the jet centre-line, one measures only the convection velocity of the foot-print of the organized structure in the shear layer; thus the convection velocity on the centre-line will be an overall convection velocity of the spot; this should be essentially that of the spot centre and thus lower than the local mean velocity. On the outer edge,

even in the zero mean flow region, the probe will sense the convection of the mixing layer large-scale coherent structure through the potential flow induced by the structure and thus the convection velocity measured will increase somewhat outwards. The highest convection velocity registered at the outer edge of the shear layer is, however, inexplicable unless it is based on two different features of the structure, when it would not represent the convection velocity of a single entity. Figure 16 tends to indicate that it is the same structure whose convection velocity is being measured except that the spot at the outer edge is being distorted so as to give the impression of acceleration.

The convection velocity profile between stations 2 and 3 appear realistic and is consistent with the expected variation in y as explained above. However, the difference between the two convection-velocity profiles is indeed drastic. The structure accelerates downstream on the high-speed side but decelerates on the low-speed side. These variations are in reasonable agreement with the convection velocity of coherent structures in an unexcited jet (Lau 1978, private communication). Bruun's (1977) data cover the range $0 \leqslant x/D \leqslant 2{\cdot}5$ only and show that convection velocities determined by positive and negative spikes of the coherent structures are distinctly different at the same η and both different from those determined through cross-correlation method. His data show that on the high-speed side the structure accelerates in x as it moves downstream while on the low-speed side it decelerates.

4. Concluding remarks

An attempt was made to understand the evolution of the three-dimensionality in an axisymmetric mixing layer by studying a spark-induced spot in the layer. Even though the spot signature is buried in the large-amplitude random turbulent signal, it was possible to educe the spot signature at three streamwise stations through signal enhancement techniques, which involved relative alignment of individual realizations through cross-correlation of low-pass filtered signals (so that turbulence-induced jitter in the spot arrival times is suppressed), rejection of realizations requiring excessive shifts, and phase averaging the aligned realizations. We do not have any clear evidence as to whether the spark induces a spot in the boundary layer preceding the nozzle lip which subsequently develops in the shear layer or it induces a large pressure pulse which directly induces a disturbance in the shear layer. We will address this aspect in part 2.

It is shown that the spot signature involves the entire mixing layer and that the spot produced noticeable turbulence. It appears that the spot is an elongated vortical structure spanning the shear-layer width. The spot travels downstream at an average convection velocity of about $0{\cdot}7U_e$, but undergoes large distortions and variations in its convection velocity near the end of the potential core. The detailed Reynolds stress, intermittency and vorticity data in the spot will be presented in part 2.

This research was supported by the National Science Foundation under grant ENG 75-15226 and the Office of Naval Research under grant 76-C-9128.

REFERENCES

ABRAMOVICH, G. N. 1963 *The Theory of Turbulent Jets.* M.I.T.

ACTON, E. 1978 *Structure and Mechanisms of Turbulence I*, vol. 75 (ed. H. Fiedler), Lecture notes in physics, p. 162. Springer.

BATT, R. G. 1975 *A.I.A.A. J.* **13**, 245.

BECHERT, D. & PFIZENMAIER, E. 1975 *J. Fluid Mech.* **72**, 341.

BIRCH, S. F. & EGGERS, J. M. 1973 *N.A.S.A.* SP-321, p. 11.

BRADSHAW, P. 1966 *J. Fluid Mech.* **26**, 225.

BROWN, G. L. & ROSHKO, A. 1974 *J. Fluid Mech.* **64**, 775.

BRUUN, H. H. 1977 *J. Fluid Mech.* **64**, 775.

CANTWELL, B. J., COLES, D. & DIMOTAKIS, P. 1978 *J. Fluid Mech.* **87**, 641.

CHAMPAGNE, F. H., PAO, Y. H. & WYGNANSKI, I. J. 1976 *J. Fluid Mech.* **74**, 209.

CHANDRSUDA, C., MEHTA, R. D., WEIR, A. D. & BRADSHAW, P. 1978 *J. Fluid Mech.* **85**, 693.

CLARK, A. R. 1974 M.S. thesis, University of Houston.

CLARK, A. R. 1979 Ph.D. dissertation, University of Houston.

COLES, D. & BARKER, S. J. 1975 *Turbulent Mixing in Nonreactive and Reactive Flows* (ed. S. N. B. Murthy), p. 285. Plenum.

CROW, S. C. & CHAMPAGNE, F. H. 1971 *J. Fluid Mech.* **48**, 547.

DAVIES, P. O. A. L. & BAXTER, D. R. J. 1978 *Structure and Mechanisms of Turbulence I*, vol. 75 (ed. H. Fiedler), Lecture notes in physics, p. 125. Springer.

DIMOTAKIS, P. E. & BROWN, G. L. 1976 *J. Fluid Mech.* **78**, 535.

FFOWCS WILLIAMS, J. E. & KEMPTON, A. J. 1978 *Structure and Mechanisms of Turbulence I*, vol. 75 (ed. H. Fiedler), Lecture notes in physics, p. 125. Springer.

FIEDLER, H. & THIES, H. J. 1978 *Structure and Mechanisms of Turbulence I*, vol. 75 (ed. H. Fiedler), Lecture notes in physics, p. 108. Springer.

FOSS, J. F. 1977 *Turbulent Shear Flows.* Pennsylvania State Univ., 11.33.

HUSAIN, Z. D. & HUSSAIN, A. K. M. F. 1979 *A.I.A.A. J.* **17**, 48.

HUSSAIN, A. K. M. F. 1978 *Structure and Mechanisms of Turbulence I*, vol. 75 (ed. H. Fiedler), Lecture notes in physics, p. 103. Springer.

HUSSAIN, A. K. M. F. & CLARK, A. R. 1977 *Physics Fluids* **20**, 1416.

HUSSAIN, A. K. M. F., KLEIS, S. J. & SOKOLOV, M. 1980 *J. Fluid Mech.* **98**, 97.

HUSSAIN, A. K. M. F. & RAMJEE, V. 1976 *Trans. A.S.M.E.* I, *J. Fluids Engng* **98**, 58.

HUSSAIN, A. K. M. F. & REYNOLDS, W. C. 1970 *J. Fluid Mech.* **41**, 241.

HUSSAIN, A. K. M. F. & ZAMAN, K. B. M. Q. 1975 *Proc. 3rd Interagency Symp. Trans. Noise, Univ. of Utah*, p. 314.

HUSSAIN, A. K. M. F. & ZAMAN, K. B. M. Q. 1978*a* *Structure and Mechanisms of Turbulence I*, vol. 75 (ed. H. Fiedler), Lecture notes in physics, p. 31. Springer.

HUSSAIN, A. K. M. F. & ZAMAN, K. B. M. Q. 1978*b* *J. Fluid Mech.* **87**, 349.

HUSSAIN, A. K. M. F. & ZEDAN, M. F. 1978*a* *Phys. Fluids* **21**. 1100.

HUSSAIN, A. K. M. F. & ZEDAN, M. F. 1978*b* *Phys. Fluids* **21**, 1475.

KLINE, S. J., REYNOLDS, W. C., SCHRAUB, F. A. & RUNSTADLER, P. W. 1967 *J. Fluid Mech.* **30**, 741.

KO, N. W. M. & DAVIES, P. O. A. L. 1971 *J. Fluid Mech.* **50**, 49.

KO, N. W. M. & KWAN, A. S. H. 1976 *J. Fluid Mech.* **73**, 305.

KOVASZNAY, L. S. G. 1978 *Structure and Mechanisms of Turbulence I*, vol. 75 (ed. H. Fiedler), Lecture notes in physics, p. 1. Springer.

LANDAHL, M. T. 1967 *J. Fluid Mech.* **29**, 441.

LAU, J. C. & FISHER, M. J. 1975 *J. Fluid Mech.* **67**, 229.

LIEPMANN, H. W. 1978 Experimental Approaches in Fluid Mechanics. Invited Lecture at *8th U.S. Nat. Cong. on Appl. Mech.* UCLA.

MICHALKE, A. & FUCHS, H. V. 1975 *J. Fluid Mech.* **70**, 179.

MOLLO-CHRISTENSEN, E. 1967 *Trans. A.S.M.E.* E, *J. Appl. Mech.* **89**, 1.

MOORE, C. J. 1977 *J. Fluid Mech.* **80**, 321.

MOORE, D. W. & SAFFMAN, P. G. 1975 *J. Fluid Mech.* **69**, 453.

PAYNE, F. R. & LUMLEY, J. L. 1967 *Physics Fluids Suppl.* **10**, S194.

PHILLIPS, O. M. 1967 *J. Fluid Mech.* **27**, 131.

REYNOLDS, W. C. & HUSSAIN, A. K. M. F. 1972 *J. Fluid Mech.* **52**, 263.

ROSHKO, A. 1976 *A.I.A.A. J.* **10**, 1349–57.

SAFFMAN, P. G. 1978 *Structure and Mechanisms of Turbulence II*, vol. 76 (ed. H. Fiedler), Lecture notes in physics, p. 273. Springer.

SCHLICHTING, H. 1968 *Boundary Layer Theory.* McGraw-Hill.

SCHUBAUER, G. B. & KLEBANOFF, P. S. 1955 *N.A.C.A. Tech. Note* TN 3489.

TOWNSEND, A. A. 1956 *The Structure of Turbulent Shear Flow.* Cambridge University Press.

WINANT, C. D. & BROWAND, F. K. 1974 *J. Fluid Mech.* **63**, 237.

WYGNANSKI, I., SOKOLOV, M. & FRIEDMAN, D. 1976 *J. Fluid Mech.* **78**, 785.

YULE, A. J. 1977 *Turb. Shear Flows.* Pennsylvania State Univ., 11.13.

ZAMAN, K. B. M. Q. 1978 Ph.D. Dissertation, University of Houston.

ZILBERMAN, M., WYGNANSKI, I. & KAPLAN, R. E. 1977 *Phys. Fluids Suppl.* **20**, S258.